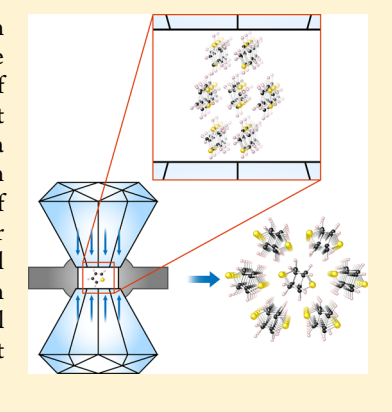
# Evidence for Orientational Order in Nanothreads Derived from Thiophene

Arani Biswas,\*,†® Matthew D. Ward,‡ Tao Wang,<sup>\$®</sup> Li Zhu,‡® Haw-Tyng Huang,<sup>\$®</sup> John V. Badding,<sup>†,§,||,⊥</sup>® Vincent H. Crespi,<sup>†,§,||</sup> and Timothy A. Strobel\*,†®

Supporting Information

Downloaded via PENNSYLVANIA STATE UNIV on December 9, 2019 at 21:48:39 (UTC). See https://pubs.acs.org/sharingguidelines for options on how to legitimately share published articles.

ABSTRACT: Nanothreads are one-dimensional sp<sup>3</sup> hydrocarbons that pack within pseudohexagonal crystalline lattices. They are believed to lack long-range order along the thread axis and also lack interthread registry. Here we investigate the phase behavior of thiophene up to 35 GPa and establish a pressure-induced phase transition sequence that mirrors previous observations in low-temperature studies. Slow compression to 35 GPa results in the formation of a recoverable saturated product with a 2D monoclinic diffraction pattern along (0001) that agrees closely with atomistic simulations for single crystals of thiophene-derived nanothreads. Paradoxically, this lower-symmetry packing signals a higher degree of structural order since it must arise from constituents with a consistent azimuthal orientation about their shared axis. The simplicity of thiophene reaction pathways (with only four carbon atoms per ring) apparently yields the first nanothreads with orientational order, a striking outcome considering that a single point defect in a 1D system can disrupt long-range structural order.



ne-dimensional sp<sup>3</sup> carbon nanothreads form by the slow, room-temperature compression and decompression of benzene<sup>1</sup> or other small aromatics<sup>2,3</sup> (unlike the amorphous products recovered from more rapid applications of pressure<sup>4,5</sup>). Their structural organization with a diamondlike tetrahedral core foreshadows the promise of novel mechanical, thermal, and optical properties.  $^{6-16}$  A nanothread lives at the juncture between crystalline rigidity and polymeric flexibility: its subnanometer width and rigid carbon-carbon cage structure make it one of the narrowest objects capable of sustaining translational and orientational order along its axis. Nonetheless, a single point defect along a nanothread can disrupt both translational and orientational order, as could domain boundaries between different on-thread structures (corresponding to different ways of interlinking successive aromatic monomers). Benzene-derived nanothreads nevertheless pack into near-single-crystal 2D pseudohexagonal lattices hundreds of microns across.<sup>17</sup> This impressively longranged order transverse to the shared nanothread axis, however, does not indicate long-ranged structural order along the axes of the constituent threads (nor registry between threads). In fact, pseudohexagonal packing suggests the opposite: nearly all fully saturated degree-6 nanothread cross sections are not hexagonal in symmetry 18 (and none of the degree-4 threads are 19), so ordered threads should pack into decidedly nonhexagonal 2D lattices. A pseudohexagonal packing should result only from threads with isotropic crosssectional shapes when averaged over the relaxation length of their torsional rigidity. Thus, the previously observed

pseudohexagonal packing suggests orientational disorder caused by structural imperfections along the lengths of individual threads, disregistry between threads, and/or possible mixtures of different thread types, which is consistent with observations from transmission electron microscopy<sup>20</sup> and atomistic simulations of nanothread packings. 17 The observation of a lower-symmetry nonhexagonal packing would provide the first indication of nanothreads with more ideal structural order.

Solid-state NMR<sup>21,22</sup> suggests that nanothread formation from benzene begins with 4 + 2 cycloaddition, a pathway also available to other small aromatics<sup>23</sup> such as pyridine<sup>2</sup> and aniline.3 Thiophene is especially intriguing as a threadproducing monomer since its four carbon atoms per ring mean that nanothread formation would terminate after only a single step on a 4 + 2 pathway (while sulfur also provides opportunities for additional functionality<sup>24–35</sup>). Such kinetic simplicity may result in more uniform reaction products, and products with higher structural quality generally provide clearer insights into structure, functionality, and formation mechanism. Here we establish the high-pressure phase diagram of molecular thiophene and show conversion to a recoverable saturated product. The product exhibits a nonhexagonal 2D lattice with a geometry that agrees closely with the results of first-principles calculations for orientationally ordered thio-

Received: August 30, 2019 Accepted: October 11, 2019 Published: October 11, 2019

<sup>†</sup>Department of Chemistry, §Department of Physics, |Department of Materials Science and Engineering, and <sup>1</sup>Materials Research Institute, The Pennsylvania State University, University Park, Pennsylvania 16802, United States

<sup>&</sup>lt;sup>‡</sup>Geophysical Laboratory, Carnegie Institution for Science, 5251 Broad Branch Road NW, Washington, D.C. 20015, United States

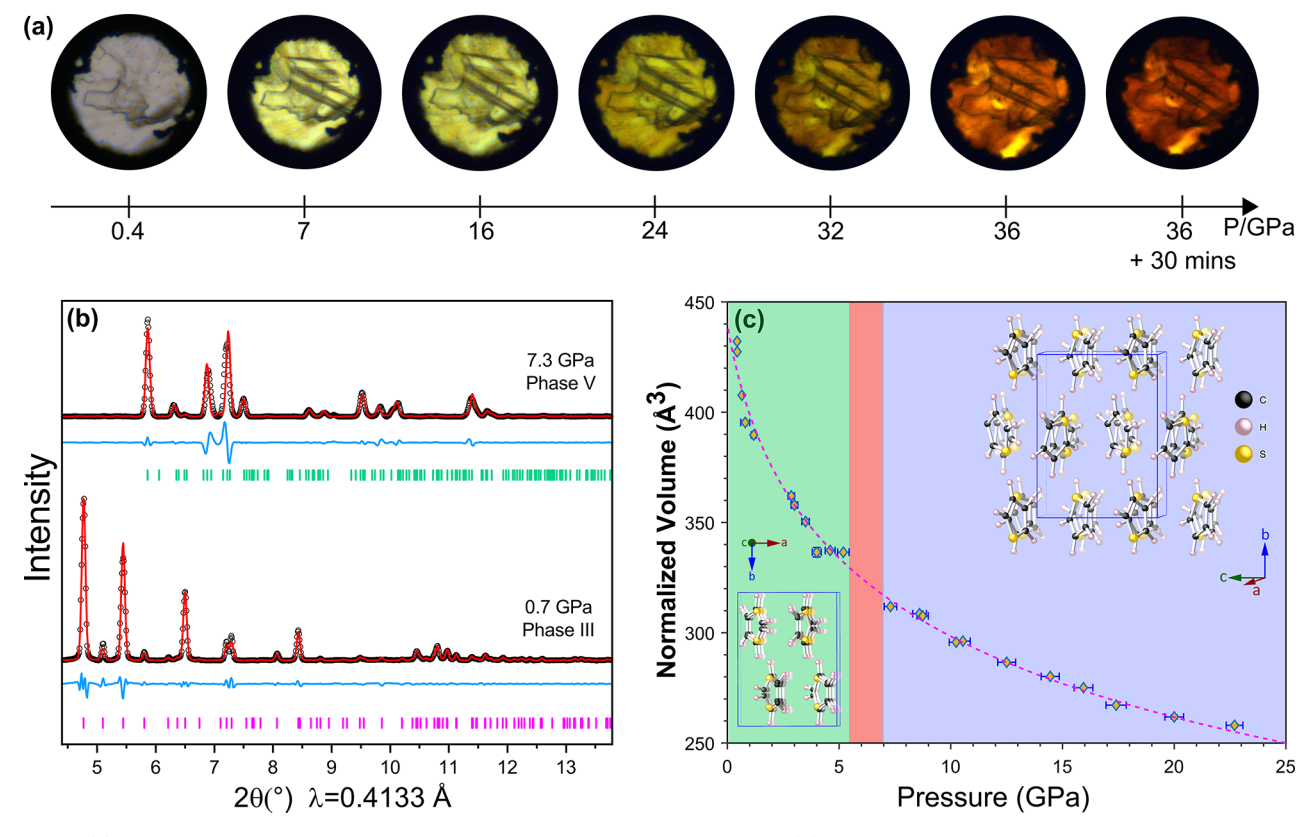


Figure 1. (a) Optical micrographs under transmitted light with increasing pressure. (b) Le Bail refinements of thiophene using two different models. Low-pressure data were best described by Phase III, while the highest-pressure data were best described by Phase V. The transition region showed larger deviations from both models, consistent with mixed phases and/or the presence of incommensurate Phase IV. (c) Equation of state for solid thiophene, with insets showing thiophene columns in Phases III and V.

phene-derived nanothreads. These observations strongly suggest that thiophene-derived threads have a consistent azimuthal orientation that is preserved over long axial distances, i.e., the first evidence of long-range orientational order in the structure of individual threads.

As samples were slowly compressed to 35 GPa over 10-12 h, the liquid froze at  $\sim 0.4$  GPa, as expected.  $^{36,37}$  Near 7 GPa, samples start taking on a yellow-orange hue, transforming to brown-amber upon approaching the final pressure of  $\sim 35$  GPa (Figure 1a). Such a color change can only occur when molecules are close to each other (less than  $\sim 3$  Å)<sup>5</sup> and indicates a reduction of optical gap. The color change was irreversible upon decompression, providing evidence of a chemical reaction.  $^{38,39}$  Before discussing this reaction product, we briefly describe the behavior of crystalline molecular thiophene prior to polymerization.

Molecular thiophene has five stable and three metastable crystalline modifications at low temperatures, <sup>36,40–44</sup> two of which (Phases II and IV) are incommensurate. <sup>42,43</sup> This complexity arises in part from the facility of thiophene to rotate about an axis perpendicular to the molecular plane. <sup>41,42</sup> Andre et al. <sup>41</sup> found crystallization to Phase I from the liquid at 0.42 GPa followed by a transition to Phase III at 0.435 GPa. Note that Andre et al. refer to Phase III as "Phase II," and a liquid—I—III triple point exists near room temperature, so the first phase to crystallize could be either I or III depending on the temperature of the room. Pruzan et al. <sup>37,45</sup> examined thiophene to 30 GPa by infrared (IR) spectroscopy, observing a molecular phase transition around 4–8 GPa and an irreversible, but incomplete chemical reaction at ~16 GPa,

recovering a white polymeric solid. Our observations confirm and refine these conclusions with the addition of structural information.

In situ single-crystal X-ray diffraction (SCXRD) was performed with synchrotron radiation at the Advanced Photon Source. The single-crystal X-ray diffraction pattern at 0.4 GPa indexes to an orthorhombic unit cell with a = 7.637(11) Å, b =10.232(4) Å, c = 5.470(9) Å, and space group *Pnma*, i.e., Phase III thiophene. 42,43 Although Andre et al. observed Phase I as the first solid phase, at room temperature the transition pressure range between I and III is vanishingly small.<sup>36,37</sup> Powder X-ray diffraction at 0.7 GPa during a separate experiment produced similar results (Figure 1b), indexing to an orthorhombic unit cell with a = 7.522(1) Å, b = 10.038(2)Å, and c = 5.399(1) Å. Both refinements agree with the literature. 42,43 At 5.2 GPa, neither single-crystal nor powder Xray diffraction could be indexed to any reported unit cell of solid thiophene. At 7.3 GPa, the X-ray pattern indexes to monoclinic Phase V. The uncertain region between 5.2 and 7.3 GPa likely results from mixed phases or could indicate incommensurate phase IV, which was observed between phases III and V at low temperature. 42,43 Since Phase V is a supercell of Phase III, the unit cell volumes in Figure 1c were scaled and fit using a third-order Birch-Murnaghan equation of state<sup>46</sup> up to 20 GPa, obtaining a zero-pressure bulk modulus  $B_0$  of 8.06  $\pm$  1.41 GPa with a first derivative  $B_0'$  =  $6.74 \pm 1.15$ . Above 20 GPa, we were unable to refine diffraction patterns likely due to nonhydrostatic stress; however, patterns remained qualitatively unchanged up to 35 GPa (i.e., a fraction of the sample remains as a molecular

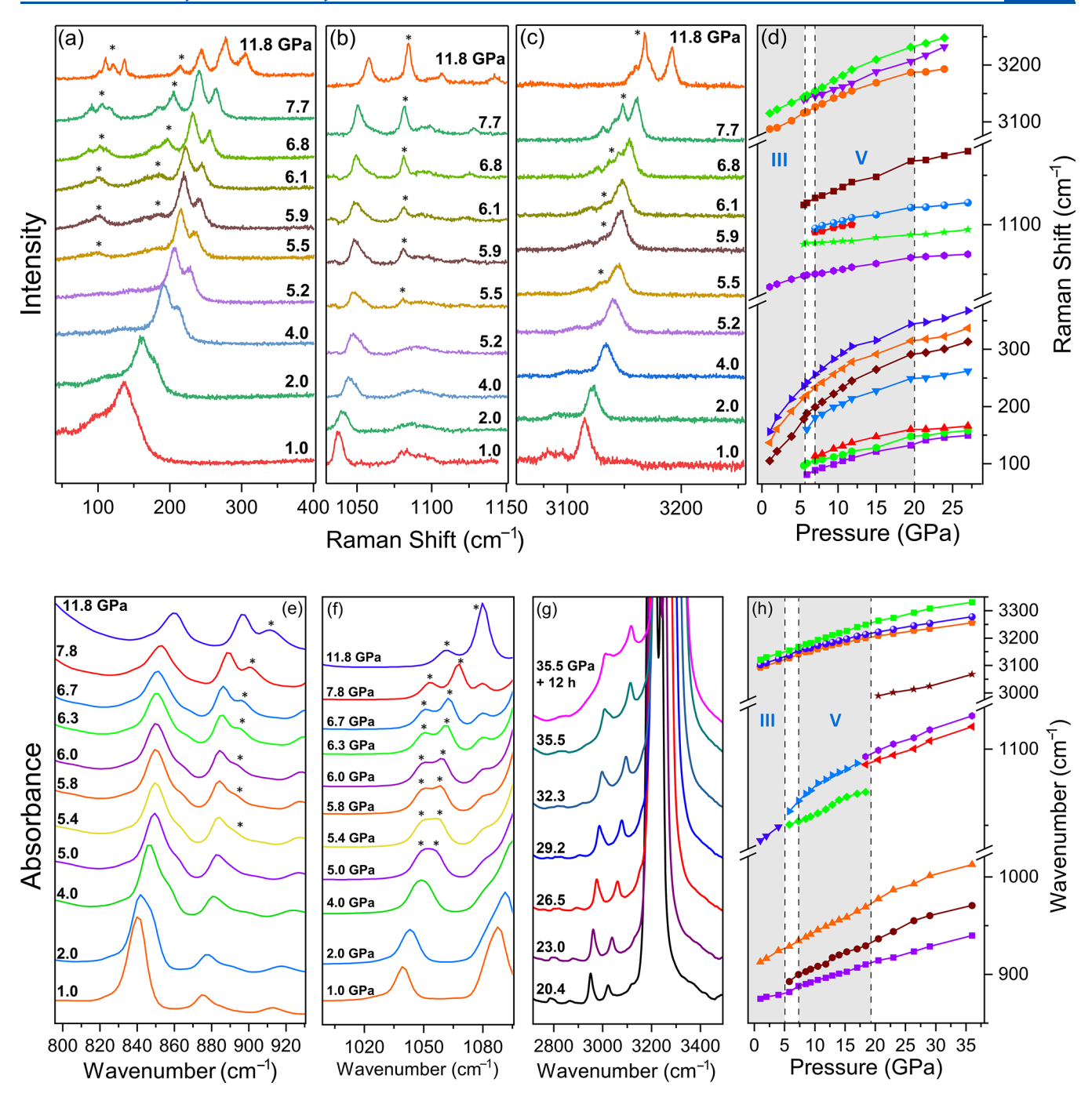


Figure 2. (a-d) In situ Raman and (e-h) FTIR spectra and vibrational frequencies of thiophene with pressure showing a phase transition at 5.5–6.2 GPa. Asterisks denote new peaks.

crystal up to the highest pressure). X-ray diffraction on decompression followed the same sequence, indicating that a portion of the transformation is reversible.

In situ vibrational spectroscopy is consistent with the diffraction results. Characteristic Raman modes of Phase III include intermolecular phonons (100–200 cm<sup>-1</sup>), ring bending (450–760 cm<sup>-1</sup>), ring stretching (830 cm<sup>-1</sup>, 1350–1430 cm<sup>-1</sup>), C–H bending (1000–1100 cm<sup>-1</sup>), and C–H stretching (3000–3100 cm<sup>-1</sup>),<sup>47,48</sup> all increasing in frequency with pressure. Around 5.5 GPa, we observed four new lattice modes between 70 and 160 cm<sup>-1</sup>, four new modes in the C–H bending region from 1070–1120 cm<sup>-1</sup>, and two new modes in the C–H stretching region from 3130–3140 cm<sup>-1</sup> (Figure

2a–d); these new peaks share similarities with low-temperature Raman spectra of Phase IV, or could indicate a sluggish transformation to Phase V.<sup>47,49</sup> Above ~6.1 GPa, the broad lattice modes split into multiple sharp peaks, closely resembling the changes observed in the low-temperature sequence from Phases III to IV to V.<sup>49</sup> Mode splitting with increasing pressure is attributed to a decrease in orientational disorder, i.e., more distinguishable local environments: Phase III is disordered, while Phase V is ordered. Overall, the sequence of molecular phases observed on increasing pressure appears analogous to that observed upon decreasing temperature.

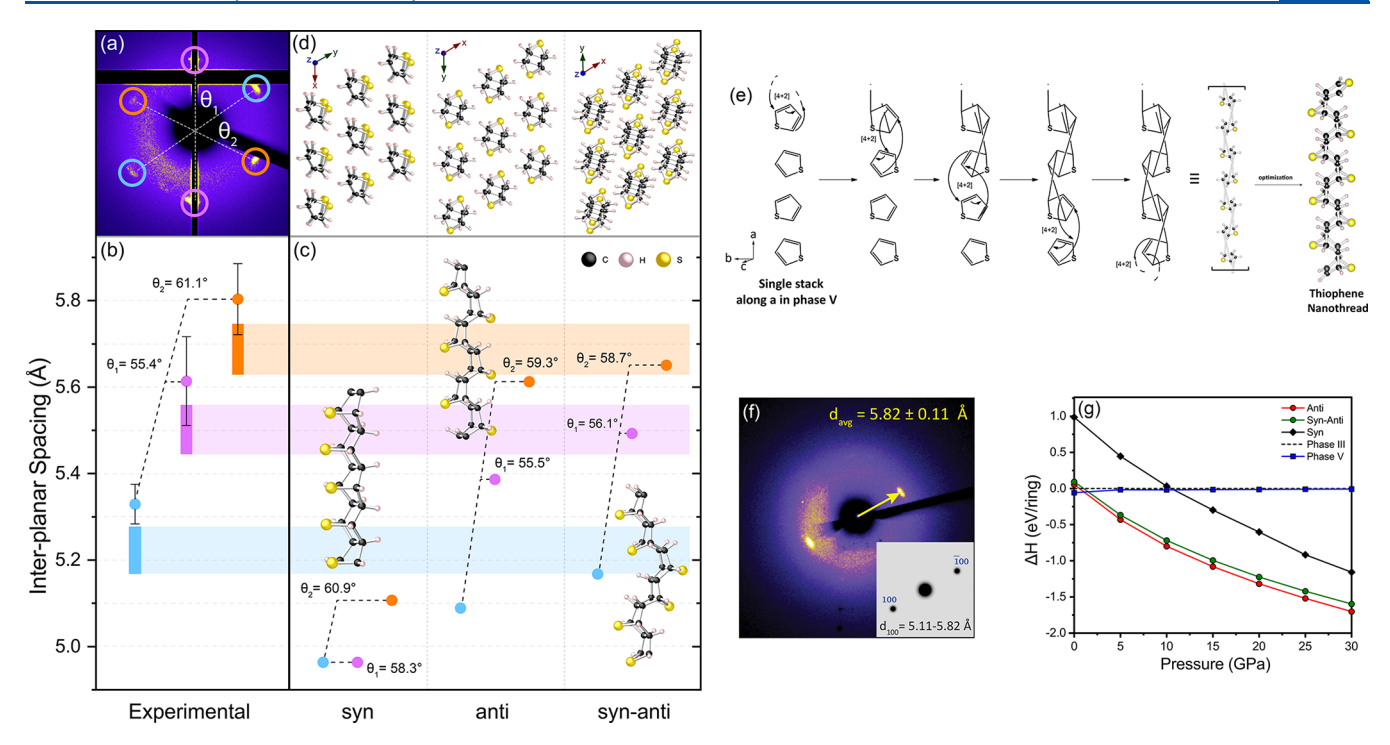


Figure 3. (a) Characteristic two-dimensional X-ray diffraction pattern of the recovered sample showing nominally 6-fold (actually monoclinic) symmetry. The black areas arise from inactive sections of the detector and shadowing from the beam stop. (b) Experimentally observed d-spacings (error-weighted averages of multiple samples with standard deviations) of each Friedel pair in the diffraction pattern at room temperature. The colors of the points correspond to the pairs circled in (a). The bars indicate the estimated range of the same d-spacings at 0 K accounting for an estimated 1–3% thermal contraction, to facilitate comparison with simulation results. (c) Friedel pair d-spacings of three model structures calculated by density functional theory, showing good agreement between the two left/right alternating structures (anti and syn-anti) and experiment. (d) Packing arrangement of each structural model within a 3 × 3 supercell, showing the orientational order. (e) Possible reaction mechanism involving [4 + 2] Diels—Alder reaction pathway resulting in the anti thiophene-derived nanothread structure. (f) XRD pattern of a recovered sample from a separate synthesis run showing 2-fold symmetry with an average d-spacing (error weighted) and simulated single-crystal diffraction pattern of the tilted anti and syn-anti models. (g) Calculated enthalpies (vdW-DFT) for molecular Phase III (reference phase), molecular Phase V, and the three nanothread models with pressure. Note that the orientational disorder of Phase III is not captured in the static DFT calculation.

Around 20 GPa, the fluorescence background increased, indicating the onset of a chemical transformation. Samples became extremely sensitive to laser irradiation at higher pressures, graphitizing via beam damage at ~0.5 mW. This sensitivity, along with the increased fluorescence background, makes it difficult to perform Raman spectroscopy (532 nm excitation) beyond ~25 GPa. To avoid this damage, we performed in situ FTIR measurements (Figures 2e-h). At lower pressures, these measurements are in excellent agreement with Raman and X-ray diffraction data, revealing for example a transition from phase III previously reported to occur between 4-8 GPa,<sup>37</sup> which can now be refined to 5.5-6.2 GPa with structural information. No additional significant changes were observed by FTIR until 20 GPa, whereupon a peak around 1090 cm<sup>-1</sup> split and a broad absorbance appeared around 2900 cm<sup>-1</sup>, below the strong sp<sup>2</sup> C-H stretching peak (Figure 2g). We assign this shoulder to sp<sup>3</sup> C-H vibrations of tetrahedrally coordinated carbon, i.e., the onset of a chemical transformation by saturation of carbon-carbon bonds. The intensity of the new sp<sup>3</sup> peak increased with pressure and also after a 12 h dwell time at 35 GPa. It strengthened further during slow decompression and persisted when the sample was released to ambient pressure. Upon opening the cell, unreacted liquid evaporated, and we recovered a dark brown solid. By comparing IR intensities of the C-H stretching region before

and after opening the cell, we estimate a reaction yield to polymerized material of  $\sim 11\%$ .

Samples recovered after slow compression and decompression show the characteristic X-ray diffraction patterns <sup>1-3,17</sup> of nanothreads: both 2-fold and what naively appear to be 6fold patterns exhibiting reflections with d-spacings at  $\sim 5-6$  Å (Figure 3). Note that these patterns reflect the ordering of constituent objects on this length scale and cannot be used for solving precise atomic positions. However, careful examination of the nominally 6-fold patterns reveals telling deviations from a hexagonal geometry. One Friedel pair is shorter than the other two (also unequal), and the angles between adjacent spots can deviate by 5 or 6 degrees from 60. This pattern of variation is consistent across multiple samples and locations therein; Figure 3b provides uncertainty-weighted averages, while the individual measurements from independent runs are provided in the Supporting Information. These deviations from hexagonal packing are too large to be explained by inhomogeneous stress and must arise from a distinct lowersymmetry crystalline packing, which requires that the constituent objects (i.e., nanothreads) have a uniform lowsymmetry cross-sectional shape. This anisotropy in crosssection is striking since a single defect in a subnanometer-wide, one-dimensional object should typically disrupt both its translational and orientational order. Consistent with this expected sensitivity to disorder, electron diffraction from

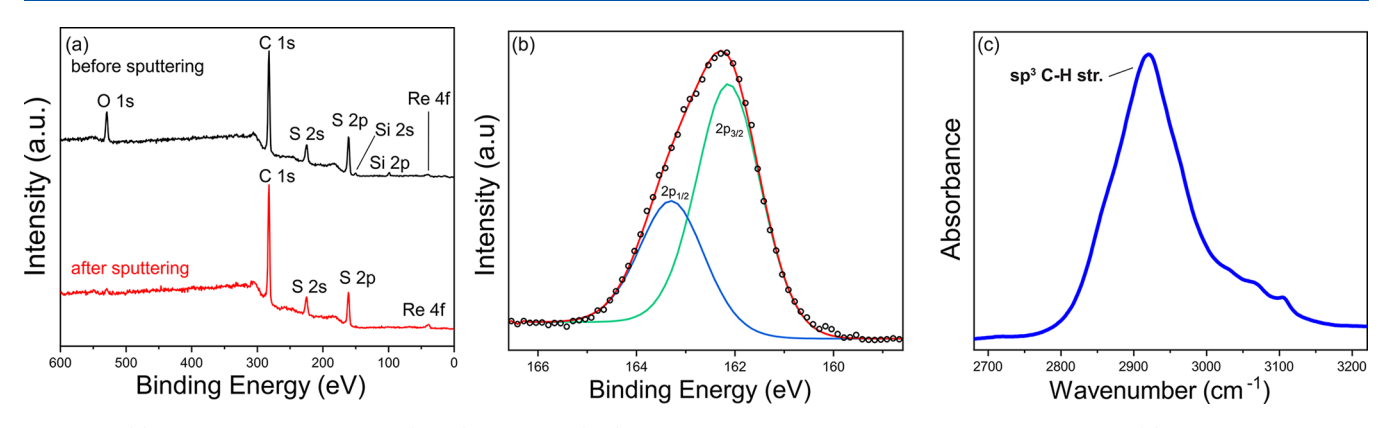


Figure 4. (a) XPS survey scans before (black) and after (red) milling shows oxidation is restricted to the surface. (b) High-resolution XPS spectrum of the S 2p peak shows that the sulfur atoms in the product reside in a saturated environment  $(2p_{3/2} \approx 162 \text{ eV})$  instead of a thiophene environment  $(2p_{3/2} \approx 164 \text{ eV})$ . (b) FTIR spectrum of the C–H stretching region in the recovered product showing predominant sp<sup>3</sup> content (<3000 cm<sup>-1</sup>).

benzene-derived nanothreads indicates a lack of interthread registry, likely reflective of structural diversity both interthread (i.e., mixtures of different degree-4 and degree-6 threads and intrathread (i.e., point defects and/or domain boundaries). Benzene-derived thread samples presumably represent an average over these variations to obtain an overall pseudohexagonal packing.

In contrast to benzene, theory suggests that thiophenederived threads should have a greatly reduced structural diversity, and—as explained below—certain plausible structural defects along a thiophene nanothread's axis preserve the orientation of the major axis of the thread's cross-section. When following the 4 + 2 cycloaddition synthetic pathway suggested by solid-state NMR of benzene-derived threads, the structure of a thiophene-derived thread is simply determined by the location of each sulfur atom relative to each successive 4 + 2 cycloaddition (Figure 3e). Following the nomenclature of Chen et al., 19 we use syn and anti to describe these spatial relationships: threads with sulfurs all on one side, alternating sides, and alternating in pairs (as shown in Figure 3c) are called syn, anti, and syn-anti, respectively. These are analogous to the IV-6, IV-7, and IV-8 degree-4 benzene threads, <sup>19</sup> upon replacing the C=C double bond with S. In the absence of ring rotations during polymerization, the anti structure follows the thiophene stacks shown in Figure 1c along the a axis of Phase V (although one should keep in mind that local structural distortions as polymerization proceeds may disrupt this simple correspondence). We also note that an off-axis diagonal polymerization pathway—such as the "para" pathway proposed for the benzene tube (3,0)<sup>19</sup>—produces nanothread structures related to the thiophene syn-anti structure. More complex syn/anti sequences are possible, but all such sequences share a common major axis to the elliptical crosssection of the thread, and the three proposed structures thus represent a broader range of potential reaction outcomes. Therefore, structural inhomogeneities in thiophene threads that form along 4 + 2 and diagonal synthetic pathways are both more limited and also much less disruptive of interthread registry than is presumably the case for benzene-derived threads. Thiophene-derived threads should thus more easily pack with a uniform alignment of their cross sections, yielding a nonhexagonal diffraction pattern. Indeed, when model threads originally packed pseudohexagonally are relaxed within a  $4 \times 4$  supercell, the optimized structures are monoclinic, with

three sets of inequivalent Friedel pairs whose d-spacings and angles closely match the experimental observations after accounting for contraction of the lattice at 0 K (Figure 3ce). This result is robust for different models of packing energetics (i.e., both first-principles + van der Waals and empirical potentials) and is consistent across multiple experimental measurements (see Supporting Information). Taken as a whole, the constrained synthetic outcomes of the polymerization pathways for thiophene, the quantitative agreement between experiment and theory for a monoclinic packing of thiophene nanothreads, and the complementary observation of a consistent 2-fold d-spacing transverse to the putative thread axis all suggest the formation of thiophenebased nanothreads with orientational order. While uncertainty remains regarding the precise chemical structure, the anti and syn-anti models represent strong candidates to understand the basic chemical structure and observed orientational order based on agreement with experiment. Enthalpies for these nanothread models as a function of pressure are shown in Figure 3g. All model structures exhibit lower energy than the molecular phases at high pressure, thus providing a thermodynamic driving force for the reaction to occur.

X-ray photoelectron spectroscopy (XPS) and FTIR provide further evidence for the largely saturated nature of the recovered product. The C/S ratio in the recovered sample was determined to be 4.97:1 by XPS, which indicates that the starting stoichiometry is maintained during the reaction (a similar preservation of stoichiometry was seen in pyridinederived threads<sup>2</sup>). The O 1s signal observed in the surface measurement disappeared after surface Ar<sup>+</sup> ion milling at 500 V for 1 min, suggesting that the observed oxygen was due to surface oxidation and is not present in the bulk (Figure 4a). The high-resolution XPS spectrum of the S 2p peak (Figure 4b) was fit to its two spin components,  $2p_{1/2}$  and  $2p_{3/2}$ . The 2p<sub>3/2</sub> peak at 162.1 eV indicates that the S atoms reside within aliphatic (-CH<sub>2</sub>-S) and not thiophenic (>164 eV) environments, 50 supporting the saturated nature of the recovered product. The most prominent feature in the IR spectrum of the recovered material (Figure S2) is an intense band between 2800-3100 cm<sup>-1</sup> assigned to C-H stretching modes (Figure 4c). The majority of this band being below 3000 cm<sup>-1</sup> provides further evidence that the recovered material is primarily a sp<sup>3</sup> bonded carbon network formed through the reaction of thiophene rings. The weak features >3000 cm<sup>-1</sup> are assigned to

sp<sup>2</sup> C-H modes of unreacted molecular thiophene or partially reacted regions such as dimers/oligomers and possible amorphous side products (such regions may also contribute to the observed brown-amber color of the recovered product).

In summary, we show that the pressure-induced phase transition sequence of molecular thiophene is analogous to that observed upon decreasing temperature. An irreversible (yet incomplete) polymerization reaction beginning at 20 GPa yields a recoverable sp<sup>3</sup>-bonded polymeric material with monoclinic order, unlike the pseudohexagonal packings seen previously for benzene- and pyridine-derived nanothreads. This lower symmetry is the likely result of a crystalline packing of one-dimensional constituents that have uniformly anisotropic (elliptical) cross sections and agrees well with structural models for the packing of thiophene-derived threads that form through a 4 + 2 cycloaddition pathway with alternating sulfur locations along the thread axis. Orientational order of thiophene-derived nanothreads, in the face of sensitivity of 1D systems to structural disruption through defects, encourages efforts toward obtaining higher degrees of synthetic control over nanothread reaction outcomes. This type of structural order is especially encouraging for future investigations related to the expression of symmetry-dependent physical properties (e.g., piezoelectricity and nonlinear optical effects). The high-pressure synthesis of ordered nanomaterials such as nanothreads can now be extended to aromatic systems with five-membered rings, a further increase in the diversity of compositions and structures achievable.

#### EXPERIMENTAL METHODS

## Sample Loading and Compression/Decompression.

Thiophene (99%), purchased from Sigma-Aldrich, was loaded along with a ruby chip in a symmetric diamond anvil cell (DAC) equipped with 400  $\mu$ m culets. The experiments were prepared by preindenting a rhenium gasket to a thickness of  $\sim$ 40  $\mu$ m, and a 150  $\mu$ m hole was drilled into the center of the indentation to serve as the sample chamber. The cell was loaded into a double-stage membrane assembly<sup>51</sup> connected to a PACE 5000 pressure controller (GE/Druck). The compression/decompression rate in the DAC was set to ~0.03-0.04 GPa/min by controlling the gas pressure in the membranes. The DAC was allowed to dwell at the final pressure of 33-35 GPa for ~10-12 h before it was decompressed. It was observed that the slow compression/ decompression rate and the high target pressure of 35 GPa was necessary to recover a crystalline product. Similar synthesis runs with faster compression/decompression rates, lower pressures, and higher temperatures (35 GPa and 200 °C) resulted in the formation of a completely amorphous material.

**X-ray Diffraction.** Synchrotron X-ray diffraction experiments were carried out at the Advanced Photon Source (APS), Argonne National Laboratory at the High Pressure Collaborative Access Team (HPCAT) at beamline 16-BMD and at GSECARS beamline 13-IDD. The cell was aligned in a focused monochromatic beam with wavelength  $\lambda = 0.4133$  or 0.3344 Å with the compression axis along the direction of the beam. The diffraction patterns were collected either on a MAR image plate or a Pilatus 1 M detector. Instrumental calibrations and pattern integrations were performed using the program DIOPTAS. Single-crystal indexing was carried out using the programs GSE-ADA and RSV, and powder patterns were refined in the programs GSAS and GSAS II. Le Bail

analysis<sup>55</sup> was implemented for the powder patterns due to incomplete powder averaging from the experimental data.

**Vibrational Spectroscopy.** Raman spectroscopy was carried out using a 532 nm diode laser focused through a  $20 \times long$  working distance objective (NA = 0.4) into the DAC. The signal was dispersed by a Princeton Instrument spectrograph SP2750 onto a  $N_2(l)$ -cooled CCD detector. The laser power was restricted between 0.5 and 1 mW to prevent any kind of sample damage. Infrared measurements were performed using a Bruker Vextex spectrometer with a Hyperion microscope and a  $N_2(l)$ -cooled midband MCT detector.

**X-ray Photoelectron Spectroscopy.** XPS experiments were performed using a Physical Electronics VersaProbe II instrument equipped with a monochromatic Al  $k\alpha$  X-ray source ( $h\nu=1,486.7$  eV) and a concentric hemispherical analyzer. Charge neutralization was performed using both low energy electrons (<5 eV) and argon ions. The binding energy axis was calibrated using sputter-cleaned Cu foil (Cu  $2p_{3/2}=932.7$  eV, Cu  $2p_{3/2}=75.1$  eV). Peaks were charge referenced to the Au  $4f_{7/2}$  band at 84.027 eV. Measurements were made at a takeoff angle of  $45^{\circ}$  with respect to the sample surface plane. This resulted in a typical sampling depth of 3-6 nm (95% of the signal originated from this depth or shallower). Quantification was done using instrumental relative sensitivity factors (RSFs) that account for the X-ray cross section and inelastic mean free path of the electrons.

#### ASSOCIATED CONTENT

# S Supporting Information

The Supporting Information is available free of charge on the ACS Publications website at DOI: 10.1021/acs.jp-clett.9b02546.

Computational methods; supporting IR and XRD analysis (PDF)
Structure files of (Syn.cif), (Syn\_Anti.cif), (Anti.cif), (Phase 3.cif), (Phase 5.cif)

### AUTHOR INFORMATION

# **Corresponding Authors**

\*E-mail: aqb5771@psu.edu (A.B.).

\*E-mail: tstrobel@carnegiescience.edu (T.A.S.).

# ORCID ®

Arani Biswas: 0000-0002-5659-7171 Tao Wang: 0000-0003-2833-1592 Li Zhu: 0000-0001-8588-9379

Haw-Tyng Huang: 0000-0002-9953-1623 John V. Badding: 0000-0002-4517-830X Timothy A. Strobel: 0000-0003-0338-4380

#### Notes

The authors declare no competing financial interest.

## ACKNOWLEDGMENTS

This work was designed and executed with support from DARPA under grant W31P4Q-13-1-0005. Computational modeling by TW/VHC and a portion of experimental work by A.B. were supported by the Center for Nanothread Chemistry, funded by the National Science Foundation (CHE-1832471). We thank C. Park, D. Popov, V. Prakapenka, and E. Greenberg of the Advanced Photon Source, Argonne National Laboratory for assistance with X-ray diffraction

measurements. Portions of this work were performed at HPCAT (Sector 16) and GSECARS (Sector 13), Advanced Photon Source (APS), Argonne National Laboratory. HPCAT operations are supported by DOE-NNSA's Office of Experimental Sciences. GeoSoilEnviroCARS is supported by the National Science Foundation - Earth Sciences (EAR -1634415) and Department of Energy—GeoSciences (DE-FG02-94ER14466). The Advanced Photon Source is a U.S. Department of Energy (DOE) Office of Science User Facility operated for the DOE Office of Science by Argonne National Laboratory under Contract No. DE-AC02-06CH11357.

## REFERENCES

- (1) Fitzgibbons, T. C.; Guthrie, M.; Xu, E. S.; Crespi, V. H.; Davidowski, S. K.; Cody, G. D.; Alem, N.; Badding, J. V. Benzene-Derived Carbon Nanothreads. *Nat. Mater.* **2015**, *14*, 43–47.
- (2) Li, X.; Wang, T.; Duan, P.; Baldini, M.; Huang, H.-T.; Chen, B.; Juhl, S. J.; Koeplinger, D.; Crespi, V. H.; Schmidt-Rohr, K.; et al. Carbon Nitride Nanothread Crystals Derived from Pyridine. *J. Am. Chem. Soc.* **2018**, *140*, 4969–4972.
- (3) Nobrega, M. M.; Teixeira-Neto, E.; Cairns, A. B.; Temperini, M. L. A.; Bini, R. One-Dimensional Diamondoid Polyaniline-Like Nanothreads from Compressed Crystal Aniline. *Chemical Science* **2018**, *9*, 254–260.
- (4) Ciabini, L.; Santoro, M.; Gorelli, F. A.; Bini, R.; Schettino, V.; Raugei, S. Triggering Dynamics of the High-Pressure Benzene Amorphization. *Nat. Mater.* **2007**, *6*, 39–43.
- (5) Shinozaki, A.; Mimura, K.; Nishida, T.; Inoue, T.; Nakano, S.; Kagi, H. Stability and Partial Oligomerization of Naphthalene under High Pressure at Room Temperature. *Chem. Phys. Lett.* **2016**, *662*, 263–267.
- (6) Roman, R. E.; Kwan, K.; Cranford, S. W. Mechanical Properties and Defect Sensitivity of Diamond Nanothreads. *Nano Lett.* **2015**, *15*, 1585–1590.
- (7) Zhang, L. W.; Ji, W. M.; Liew, K. M. Mechanical Properties of Diamond Nanothread Reinforced Polymer Composites. *Carbon* **2018**, 132, 232–240.
- (8) Zhan, H.; Zhang, G.; Bell, J. M.; Gu, Y. The Morphology and Temperature Dependent Tensile Properties of Diamond Nanothreads. *Carbon* **2016**, *107*, 304–309.
- (9) Silveira, J. F. R. V.; Muniz, A. R. First-Principles Calculation of the Mechanical Properties of Diamond Nanothreads. *Carbon* **2017**, *113*, 260–265.
- (10) Zhan, H.; Zhang, G.; Zhang, Y.; Tan, V. B. C.; Bell, J. M.; Gu, Y. Thermal Conductivity of a New Carbon Nanotube Analog: The Diamond Nanothread. *Carbon* **2016**, *98*, 232–237.
- (11) Zhan, H.; Zhang, G.; Tan, V. B. C.; Cheng, Y.; Bell, J. M.; Zhang, Y.-W.; Gu, Y. Diamond Nanothread as a New Reinforcement for Nanocomposites. *Adv. Funct. Mater.* **2016**, *26* (29), 5279–5283.
- (12) Zhan, H.; Zhang, G.; Tan, V. B. C.; Gu, Y. The Best Features of Diamond Nanothread for Nanofibre Applications. *Nat. Commun.* **2017**, *8*, 14863.
- (13) Gryn'ova, G.; Corminboeuf, C. Topology-Driven Single-Molecule Conductance of Carbon Nanothreads. J. Phys. Chem. Lett. **2019**, 10 (4), 825–830.
- (14) Demingos, P. G.; Muniz, A. R. Electronic and Mechanical Properties of Partially Saturated Carbon and Carbon Nitride Nanothreads. *J. Phys. Chem. C* **2019**, *123* (6), 3886–3891.
- (15) Marutheeswaran, S.; Jemmis, E. D. Adamantane-Derived Carbon Nanothreads: High Structural Stability and Mechanical Strength. *J. Phys. Chem. C* **2018**, *122* (14), 7945–7950.
- (16) Wu, W.; Tai, B.; Guan, S.; Yang, S. A.; Zhang, G. Hybrid Structures and Strain-Tunable Electronic Properties of Carbon Nanothreads. J. Phys. Chem. C 2018, 122 (5), 3101–3106.
- (17) Li, X.; Baldini, M.; Wang, T.; Chen, B.; Xu, E. S.; Vermilyea, B.; Crespi, V. H.; Hoffmann, R.; Molaison, J. J.; Tulk, C. A.; et al. Mechanochemical Synthesis of Carbon Nanothread Single Crystals. *J. Am. Chem. Soc.* **2017**, *139*, 16343–16349.

- (18) Xu, E.-s.; Lammert, P. E.; Crespi, V. H. Systematic Enumeration of sp3 Nanothreads. *Nano Lett.* **2015**, *15* (8), 5124–5130.
- (19) Chen, B.; Hoffmann, R.; Ashcroft, N. W.; Badding, J.; Xu, E.; Crespi, V. Linearly Polymerized Benzene Arrays as Intermediates, Tracing Pathways to Carbon Nanothreads. *J. Am. Chem. Soc.* **2015**, 137 (45), 14373–14386.
- (20) Juhl, S. J.; Wang, T.; Vermilyea, B.; Li, X.; Crespi, V. H.; Badding, J. V.; Alem, N. Local Structure and Bonding of Carbon Nanothreads Probed by High-Resolution Transmission Electron Microscopy. *J. Am. Chem. Soc.* **2019**, *141* (17), 6937–6945.
- (21) Duan, P.; Li, X.; Wang, T.; Chen, B.; Juhl, S. J.; Koeplinger, D.; Crespi, V. H.; Badding, J. V.; Schmidt-Rohr, K. The Chemical Structure of Carbon Nanothreads Analyzed by Advanced Solid-State Nmr. J. Am. Chem. Soc. 2018, 140 (24), 7658–7666.
- (22) Wang, T.; Duan, P.; Xu, E.-S.; Vermilyea, B.; Chen, B.; Li, X.; Badding, J. V.; Schmidt-Rohr, K.; Crespi, V. H. Constraining Carbon Nanothread Structures by Experimental and Calculated Nuclear Magnetic Resonance Spectra. *Nano Lett.* **2018**, *18* (8), 4934–4942.
- (23) Silveira, J. F. R. V.; Muniz, A. R. Functionalized Diamond Nanothreads from Benzene Derivatives. *Phys. Chem. Chem. Phys.* **2017**, *19*, 7132–7137.
- (24) Ebnesajjad, S. Characteristics of Adhesive Materials. In *Handbook of Adhesives and Surface Preparation*; Elsevier: 2011; pp 137–183.
- (25) Garnier, F.; Tourillon, G.; Gazard, M.; Dubois, J. C. Organic Conducting Polymers Derived from Substituted Thiophenes as Electrochromic Material. *J. Electroanal. Chem. Interfacial Electrochem.* 1983, 148 (2), 299–303.
- (26) Kaneto, K.; Yoshino, K.; Inuishi, Y. Electrical Properties of Conducting Polymer, Poly-Thiophene, Prepared by Electrochemical Polymerization. *Jpn. J. Appl. Phys.* **1982**, *21*, L567–L568.
- (27) Kato, M.; Toshima, K.; Matsumura, S. Enzymatic Synthesis of Polythioester by the Ring-Opening Polymerization of Cyclic Thioester. *Biomacromolecules* **2007**, *8* (11), 3590–3596.
- (28) Kawada, J.; Lütke-Eversloh, T.; Steinbüchel, A.; Marchessault, R. H. Physical Properties of Microbial Polythioesters: Characterization of Poly(3-Mercaptoalkanoates) Synthesized by Engineered Escherichia Coli. *Biomacromolecules* **2003**, *4* (6), 1698–1702.
- (29) Kultys, A. Sulfur-Containing Polymers. In Encyclopedia of Polymer Science and Technology; Wiley: 2010.
- (30) Luo, M.; Zhang, X.-H.; Darensbourg, D. J. Poly-(Monothiocarbonate)S from the Alternating and Regioselective Copolymerization of Carbonyl Sulfide with Epoxides. *Acc. Chem. Res.* **2016**, *49*, 2209–2219.
- (31) Odaci, D.; Kiralp Kayahan, S.; Timur, S.; Toppare, L. Use of a Thiophene-Based Conducting Polymer in Microbial Biosensing. *Electrochim. Acta* **2008**, *53*, 4104–4108.
- (32) Okutan, M.; Yerli, Y.; San, S. E.; Yilmaz, F.; Günaydin, O.; Durak, M. Dielectric Properties of Thiophene Based Conducting Polymers. *Synth. Met.* **2007**, *157*, 368–373.
- (33) Roudini, D. Synthesis and Properties of Novel Thiophene-Based Liquid Crystalline Conducting Polymers. *Polym. Polym. Compos.* **2017**, *25*, 669–676.
- (34) So, J. H.; Mayevsky, D.; Winther-Jensen, O.; Winther-Jensen, B. A Novel Route for Polymerisation of Thiophene Based Conducting Polymers Using Trace-Free Oxidants. *Polym. Chem.* **2014**, *5*, 361–364.
- (35) Zhang, H. Waterproof Materials. In *Building Materials in Civil Engineering*; Elsevier: 2011; pp 253–423.
- (36) Andre, D.; Szwarc, H. Phase Transitions and Dynamics Driven Incommensurability in Thiophene. *Phase Transitions* **1991**, *31*, 59–74.
- (37) Pruzan, P.; Chervin, J. C.; Forgerit, J. P. Chemical and Phase Transformations of Thiophene at High Pressures. *J. Chem. Phys.* **1992**, 96, 761–767.
- (38) Armour, M.; Davies, A. G.; Upadhyay, J.; Wassermann, A. Colored Electrically Conducting Polymers from Furan, Pyrrole, and Thiophene. J. Polym. Sci., Part A-1: Polym. Chem. 1967, 5, 1527–1538.

- (39) Meisel, S. L.; Johnson, G. C.; Hartough, H. D. Polymerization of Thiophene and Alkylthiophenes. *J. Am. Chem. Soc.* **1950**, 72, 1910–1912.
- (40) Abrahams, S. C.; Lipscomb, W. N. The Crystal Structure of Thiophene at  $-55^{\circ}$  C. Acta Crystallogr. 1952, 5, 93–99.
- (41) Andre, D.; Figuiere, P.; Fourme, R.; Ghelfenstein, M.; Labarre, D.; Szwarc, H. Crystalline Thiophene-I. Phase Diagram and Structures of Two Orientationally Disordered Crystalline Phases. Crystallographic Evidence for a Metastable Low Temperature Phase. *J. Phys. Chem. Solids* 1984, 45, 299–309.
- (42) Damay, F.; Rodríguez-Carvajal, J.; André, D.; Dunstetter, F.; Szwarc, H. Orientational Ordering in the Low-Temperature Stable Phases of Deuterated Thiophene. *Acta Crystallogr., Sect. B: Struct. Sci.* **2008**, *64*, 589–595.
- (43) Dunstetter, F.; André, D.; Gonthier-Vassal, A.; Szwarc, H.; Ratovelomanana, N.; Lautie, M. F. Observation of an Incommensurate Phase in the Stable Phase Sequence of Deuterated Thiophene by Powder Neutron Diffraction. *Chem. Phys.* **1993**, *175*, 475–482.
- (44) Migliorini, M. G.; Salvi, P. R.; Sbrana, G. New Spectroscopic Evidence of the Four Solid Modifications of Thiophene. *Chem. Phys. Lett.* **1974**, 28, 565–568.
- (45) Pruzan, P.; Chervin, J. C.; Forgerit, J. P. Infrared Spectroscopy of Thiophene up to 30 GPa. Polymerization after a Pressure! Cycle to 16 GPa. *High Pressure Res.* **1992**, *9*, 255–258.
- (46) Ahmad, J. F.; Alkammash, I. Y. Theoretical Study of Some Thermodynamical Properties for Solid under High Pressure Using Finite-Strain Eos. J. Assoc. Arab Univ. Basic Appl. Sci. 2012, 12, 17–22.
- (47) Andre, D.; Dworkin, A.; Figuiere, P.; Fuchs, A. H.; Szwarc, H. Crystalline Thiophene. Ii: A Comprehensive Study of Stable and Metastable Phases by Means of Heat Capacity, Thermally Stimulated Currents and Raman Spectroscopy Measurements. *J. Phys. Chem. Solids* 1985, 46, 505–513.
- (48) Shimizu, H.; Matsunami, N. High-Pressure Raman Study of Liquid and Solid Thiophene up to 100 Kbar at 300 K. J. Raman Spectrosc. 1988, 19, 199–201.
- (49) Colombo, L.; Kirin, D.; Furić, K.; Sullivan, J. F.; Durig, J. R. Far Infrared and Raman Spectroscopic Investigations of the Lattice Modes of Crystalline Thiophene. *Croatica Chemica Acta* **1988**, 61, 301–311
- (50) Lindberg, B J; Hamrin, K; Johansson, G; Gelius, U; Fahlman, A; Nordling, C; Siegbahn, K Molecular Spectroscopy by Means of Esca Ii. Sulfur Compounds. Correlation of Electron Binding Energy with Structure. *Phys. Scr.* **1970**, *1*, 286–298.
- (51) Sinogeikin, S. V.; Smith, J. S.; Rod, E.; Lin, C.; Kenney-Benson, C.; Shen, G. Online Remote Control Systems for Static and Dynamic Compression and Decompression Using Diamond Anvil Cells. *Rev. Sci. Instrum.* **2015**, *86* (7), 072209.
- (52) Prescher, C.; Prakapenka, V. B. Dioptas: A Program for Reduction of Two-Dimensional X-Ray Diffraction Data and Data Exploration. *High Pressure Res.* **2015**, *35*, 223–230.
- (53) Dera, P.; Zhuravlev, K.; Prakapenka, V.; Rivers, M. L.; Finkelstein, G. J.; Grubor-Urosevic, O.; Tschauner, O.; Clark, S. M.; Downs, R. T. High Pressure Single-Crystal Micro X-Ray Diffraction Analysis with Gse\_Ada/Rsv Software. *High Pressure Res.* **2013**, 33, 466–484.
- (54) Toby, B. H.; Von Dreele, R. B. Gsas-Ii: The Genesis of a Modern Open-Source All Purpose Crystallography Software Package. *J. Appl. Crystallogr.* **2013**, *46*, 544–549.
- (55) Le Bail, A. Espoir: A Program for Solving Structures by Monte Carlo Analysis of Powder Diffraction Data. *Mater. Sci. Forum* **2001**, 378–381, 65–70.